CCFE
CULHAM CENTRE FOR FUSION ENERGY

UK Atomic Energy Authority

UKAEA-CCFE-PR(23)104

S.F. Smith, A. Kirk, B. Chapman, J. G. Clark, C.J. Ham, L. Horvath, C. F. Maggi, R. Scannell, S. Saarelma

Studying pedestal characteristics in MAST ELMy regimes in preparation for future spherical tokamaks

Studying pedestal characteristics in MAST ELMy regimes in preparation for future spherical tokamaks

S.F. Smith, A. Kirk, B. Chapman, J. G. Clark, C.J. Ham, L. Horvath, C. F. Maggi, R. Scannell, S. Saarelma

This is a preprint of a paper submitted for publication in Plasma Physics and Controlled Fusion

Studying pedestal characteristics in MAST ELMy regimes in preparation for future spherical tokamaks

S.F. Smith[1], A. Kirk[1], B. Chapman[1], J. G. Clark[1,2], C.J. Ham[1], L. Horvath[1], C. F. Maggi[1], R. Scannell[1], S. Saarelma[1] and the MAST Team

[1] *CCFE, Culham Science Centre, Abingdon, Oxon, UK.*
[2] *Department of Electrical Engineering and Electronics, University of Liverpool, Liverpool L69 3GJ, United Kingdom.*

ABSTRACT

MAST pedestal data has been analysed, where a pedestal database of 892 shots was obtained, using the new upgraded MAST Thomson Scattering (TS) diagnostic. Various ELM types are discussed, where characteristics and trends of MAST pedestals are shown. The data from the upgraded TS diagnostic confirms pedestal characteristics found in earlier analysis, using previous TS systems. Using the database, calculations of the bootstrap current are obtained using the different analytical formulae (Sauter and Redl), and comparisons are performed. At high collisionality discrepancies between the analytical calculations are found for MAST. The new MAST TS system now spans the full plasma mid-plane, such that direct comparisons between inboard and outboard pedestals can be obtained. When the inboard and outboard pedestals are compared, asymmetries in the density pedestal width are found. In order to increase confidence in spherical tokamak pedestal predictions, the assumptions of Europed have been validated for MAST pedestal data. Using the experimental database for type I ELMs in single and double null configurations, a value for the KBM constraint (C) has been obtained. Here, it was found $C \sim 0.145$. Using this value, the first spherical tokamak pedestal predictions were performed in Europed and compared to MAST experimental data. The temperature pedestal height was predicted to within 10% error of the experimental value. In addition type II ELMs on MAST are analysed, and stability analysis and parameter scans have been performed using ESSIVE. Similar MHD stability properties are observed for type I and type II ELMs, originating from the mixed ELM regimes, and it is therefore difficult to distinguish these ELMs using the ideal MHD codes.

1 Introduction

Currently, the favoured operating regime for a tokamak is the high confinement mode (H-mode) [1], where increased core plasma pressure is encouraging but edge localised mode (ELM) instabilities occur, and are an issue. Filaments are ejected from the plasma when an ELM occurs [2] transporting energy and particles to the divertor region, resulting in a loss in the pedestal energy confinement [3]. Large and uncontrolled type I ELMs on future tokamaks, such as ITER, will generate high enough heat fluxes to damage machine facing components [4]. It is therefore important, for future devices, to understand the conditions under which type I ELM instabilities occur and to make reliable pedestal predictions in order to completely avoid large ELMs, especially if ELM mitigation or suppression is not possible. Exploration and development of ELM free operational regimes or regimes with small ELMs is also underway [5].

The Mega Ampere Spherical Tokamak (MAST), a low aspect ratio tokamak based at Culham in the UK, operated from 2000-2013 and has recently undergone an upgrade to MAST-U [6]. Pedestal data from the final 3 physics campaigns on MAST, obtained using the new upgraded Thomson Scattering (TS) diagnostic [7], is analysed here in anticipation of the initial MAST-U experiments. The data analysed from this former tokamak can inform spherical tokamak pedestal research, contribute to the understanding of MAST-U pedestal experiments, and to the knowledge of pedestal characteristics for future spherical tokamaks, such as STEP [8].

Previous MAST pedestal data has been analysed in [9–11], where a wide range of ELM regimes has been observed. The most common is the type I ELM regime, with type III ELMs also occurring in many discharges, and a branch of the type III ELMs, also referred to as type IV ELMs were found, appearing in low collisionality plasmas [12]. The MAST pedestal database is obtained, as described in section 2. In section 3 analysis of the pedestal database is performed and includes an overview of the database for the different ELM types in section 3.1. The data from the upgraded TS diagnostic confirms pedestal characteristics found in earlier analysis, using previous TS systems. The upgraded TS system views the entire plasma mid-plane from the high-field-side (HFS) to the low-field-side (LFS). In section 3.2 a direct comparison has been performed between the HFS and LFS data in the lower single null (SN) and connected double null (DN) configurations.

Analytical formulae used to calculate the bootstrap current from Sauter [13] and Redl [14], have been used here for the MAST pedestal database. A comparison of the calculations of the peak edge current density (j_{peak}) is given in section 3.3. Calculations of j_{peak} using both formulae have also been performed in the HELENA code [15] and compared to the experimental data.

Accurate pedestal predictions are important in order to obtain a boundary condition for core transport simulations, that can predict the performance of the plasma. Europed [16] can be used for predictions of peeling-ballooning (P-B) limited pedestals. It is based on the EPED1 model [17], where the pedestal height and width can be predicted. EPED predictions have been obtained on various conventional tokamaks [18], and more recently predictions for MAST pedestals have been performed [19]. However, it is still important to analyse the MAST data to verify whether the Europed/EPED model assumptions are valid for MAST and spherical tokamaks in general. This is investigated in section 4, where it has been possible to determine Europed input parameters from the experimental database and use these for first spherical tokamak pedestal predictions using Europed.

The type I ELM analysis is useful for avoiding such large ELM regimes by finding P-B pedestal limits, but research is also performed on other operating regimes, which could be used in future spherical tokamaks, such as STEP. The type II ELM regime is a potential operating regime where the ELM instabilities are smaller than the type I ELMs. Type II ELMs are observed in specific circumstances in MAST plasmas [20]. These small ELM regimes release a few percent of the pedestal energy and have been observed in highly shaped, high pedestal density plasmas in various tokamaks including JET [21], ASDEX-Upgrade [22, 23] and NSTX [24]. In section 5 MAST type II pedestal characteristics are discussed, using data from the TS diagnostic and fast camera images. Ideal MHD stability analysis is also performed for the type II ELMs using ESSIVE, and a comparison is made to the type I ELMs. Finally a summary and conclusions are given in section 6.

2 Obtaining the MAST pedestal database

From 2007 to 2013 the final 3 campaigns took place at MAST, this paper aims to investigate the pedestal characteristics from these MAST campaigns, in preparation for the new physics campaigns on MAST-U and to support the development of STEP. The database includes over 800 shots, where an ELMy H-mode has been obtained, in either a lower single null (SN) or double null (DN) configuration. Typical MAST SN and DN configurations are shown in [11]. In the DN configuration the two x-points are roughly on the same flux surface. From the database, the gap between these surfaces at the outboard mid-plane (δr_{sep}) is no larger than 6.5 mm.

The database contains a range of shots with various plasma parameters. From the database, MAST plasmas typically have a major radius of R $\sim$ 0.85 m and a minor radius, a $\sim$ 0.55 m. The toroidal magnetic field on axis (B_T) ranges from 0.3-0.5 T, the plasma current (I_p) $\sim$0.4-1.0 MA, the Greenwald density $\sim$0.3-0.95, the safety factor at 95% of flux surface q_{95} $\sim$2-9 and the heating power from neutral beam injection (NBI) is $\sim$1.0-3.8

MW. The plasma shaping parameters are over a range of values, elongation κ ~1.4-2.1 and the average triangularity (ie. $(\delta = (\delta_u + \delta_l)/2.0)$, δ ~0.25-0.53.

The upgraded Thomson Scattering (TS) system [7] on MAST, was used to measure the electron density (n_e) and temperature (T_e) profiles across MAST plasmas. The system uses eight Nd:YAG lasers, each with a repetition rate of 30 Hz. This upgrade enhanced the previous edge Nd:YAG [25] and Ruby TS [26] systems. The Nd:YAG laser is located 14.5 mm above the centre of the machine, with 130 points radially across giving a spatial resolution of $\sim$ 1cm. In the SN configuration the laser beams are approximately 30 cm above the height (z) of the magnetic axis of the plasma. In the DN configuration the laser beams are approximately the at the height of the magnetic axis. For comparison between pedestal widths in DN and SN discharges the SN profiles are mapped to the z location of the magnetic axis. The TS system on MAST allows for measurements, at the mid-plane, radially across the whole plasma, allowing for comparisons of the low-field-side and high-field-side pedestals in both the SN and DN configurations.

Examples of typical time traces of MAST shots are shown in fig. 1. For a visual comparison of the ELM phases, the time axes have been offset for each pulse to approximately the start of the H-mode period, characterised by a drop in the D_α signal. The plasma current, neutral beam power, core electron temperature and line averaged density are given in figs. 1a)-d) respectively, showing the steady state period. The D_α trace for a SN discharge is given in fig. 1e), where only type I ELMs are observed. Fig. 1f) shows the D_α trace for a DN discharge where type III ELMs are observed at the start of H-mode, after a transition occurs to type I ELMs. In fig. 1g) another DN discharge is shown. From $\sim$ 0.1 s periods of small type II ELMs are observed, these are interspersed with type I ELMs. For the database, MAST H-mode shots were first identified, and then using the D_α trace of a discharge, it was possible to collect the data for the observed ELM-y regime.

When the data is collected the first ELM is neglected, as it is not representative of the following ELMs. Prior to the first ELM a dramatic increase of the edge density, above the central density, is observed [27]. Therefore, the collection of data starts after the first ELM until the last ELM or for the duration of the steady state. For each TS point within this period the profile data for n_e and T_e is included in the database. The data points that occur 0.2 ms before and after an ELM are removed from the database. To study certain pedestal characteristics a cut can be introduced to only include the TS data from the final 25% of the ELM cycle, just before the ELM. At this stage, and for the analysis in section 3, the data is not ELM averaged, due to the low number of ELMs per shot. The data has been ELM averaged at a later stage for the pedestal prediction studies (section 4). The TS pedestal data is then fitted with a modified hyperbolic tangent (mtanh) function [28] to obtain the

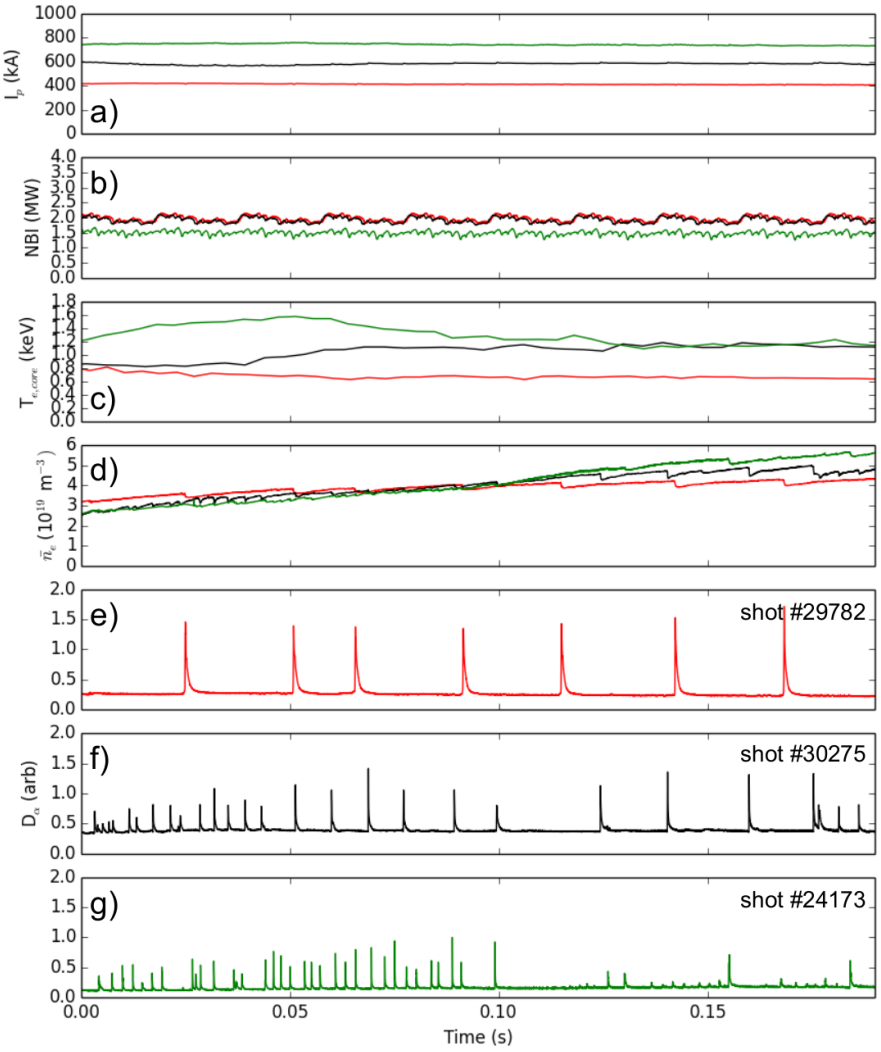

Figure 1: *Time traces for three MAST shots, showing the plasma current, neutral beam power, the core temperature, the averaged line density and the D_α traces. The red line is a type I ELM regime in the SN configuration, the black lines shows the traces for a DN configuration and the green a type II interspersed with type I in a DN configuration.*

pedestal parameters (i.e. the pedestal height $X_{e,ped}$, pedestal width ΔX_e, pedestal position $X_{e,pos}$ for the density, temperature and pressure). Examples of the TS data and the typical fits to the pedestal profiles are given for n_e and T_e in fig. 2.

For MAST plasmas, comparisons of T_i profiles from CXRS and T_e profiles from the TS system were performed in [29, 30]. It was found that $T_i = T_e$ in the core, inside the pedestal region. At the pedestal in high collisionality plasmas this is also a good approximation. In low collisionality plasmas at the pedestal top $T_i \sim T_e$ but the gradient of the ion temperature is shallower than the electron temperature so $T_i > T_e$ at the separatrix. Therefore in MAST plasmas, the assumption that $T_i = T_e$ is valid for certain collisionalities and is in general valid at the pedestal top. The total thermal (ion and electron) pressure at the top of the pedestal (p_{ped}) is determined as $p_{ped} = p_{e,ped} + p_{i,ped}$, we use $T_i = T_e$ and the ion density is

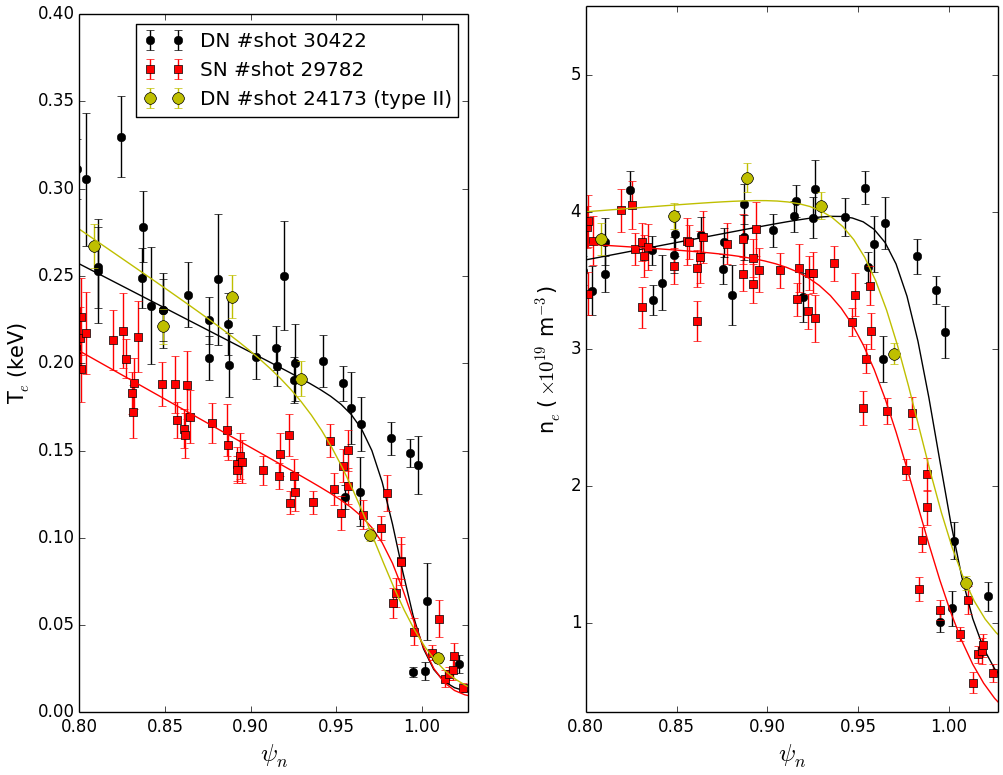

(a) (b)

Figure 2: *Examples of Thomson Scattering profiles for a) the temperature and b) the density. Profiles for type I ELMs are ELM averaged using profiles in the final 25% of the cycle, the type II ELM is a single TS profile in the final 25% of the ELM cycle.*

determined from n_e and Z_{eff}, with carbon as the main impurity.

The database contains a wide range of density and temperature pedestals, where the pedestal heights are in the range $n_{e,ped}$ = 1.2-6.5×10^{19} m^{-3} and $T_{e,ped}$ = 50-300 eV, where the various ELM types occur. The pedestal values can be used to calculate the collisionality (ν_e^*), normalised pedestal pressure (β_{ped}), the normalised pressure gradient (α) and the ELM energy loss ($\Delta W/W_{ped}$).

The SN discharges are dominated by type I ELMs, in comparison to the DN shots, where a variety of ELM types occur. To distinguish the type I and type III ELMs, previous studies on MAST [11] were used. When the ELM frequency is observed as a function of increasing input power a minimum in the ELM frequency for pedestal temperatures of 150 eV was previously found. An associated transition from type III ELMs to type I ELMs occurs at this pedestal temperature. Another high frequency ELM regime, type IV ELMs, occurs on MAST at higher temperatures and lower densities ($n_e < 2.5 \times 10^{19}$ m^{-3}) than the type III ELMs, also known as the low collisionality branch of the type III ELMs. The type IV ELMs are obtained on MAST with beam powers over 3 MW and an optimised fuelling scenario

[11].

Using a combination of D_α traces and high time resolution fast camera images, we are able to distinguish type II ELMs by their more numerous and uniform filamentary structures compared to other ELM types [20]. Only a limited set of type II ELM data was collected and verified due to the lack of type II ELM shots in the final 3 campaigns on MAST, and also the limited high time resolution fast camera images, used for verification.

3 Analysing the MAST pedestal database

From the final 3 MAST campaigns 892 shots with 19,480 TS time points have been collected. By analysing this MAST ELM-y H-mode database, pedestal characteristics can be determined. In this section an overview of the database is given, including different ELM types and plasma configurations, comparisons between the inboard and outboard pedestals are performed, and bootstrap current calculations investigated. The type II ELM data is analysed separately in section 5.

3.1 Overview of pedestal data

From the database, the pedestal electron temperature ($T_{e,ped}$) and density ($n_{e,ped}$) for all the profiles in the last 25% of the ELM cycle are given in fig. 3a). A wide range of pedestal values are seen for the type I ELMs in SN and DN configurations. The type III ELMs occur at lower $T_{e,ped}$ over a range of $n_{e,ped}$, whilst the type IV ELMs occur at lower $n_{e,ped}$ over a range of $T_{e,ped}$.

Pedestals that are unstable to type I ELMs are thought to be limited by peeling-ballooning modes, which are driven by steep pressure gradients and large current density in the edge [31]. Fig. 3b) shows the distribution of the MAST pedestal data from the final 25% of the ELM cycle, in j-α space. j_{peak} is the peak parallel current density in the pedestal region, calculated from the addition of the Ohmic current profile from the equilibrium and the contribution from the bootstrap current profile. The bootstrap current has been calculated here from the Sauter formula [13], using the outboard density and temperature profiles. α_{max} is the normalised pressure gradient calculated using the equation in [32]. Fig. 3b) shows the type I ELMs in the DN configuration are located at higher j_{peak} and α_{max} associated with the peeling-ballooning boundary. In general, a higher plasma current was required for the DN shots, therefore, higher temperature pedestals were obtained. The SN shots occur over a range of $T_{e,ped}$, α_{max} and j_{peak}, as seen in fig. 3a)&b).

The high collisionality type III ELMs are thought to be due to resistive ballooning modes [11, 33], in fig. 3b), they are located at a lower current density but can be found at higher

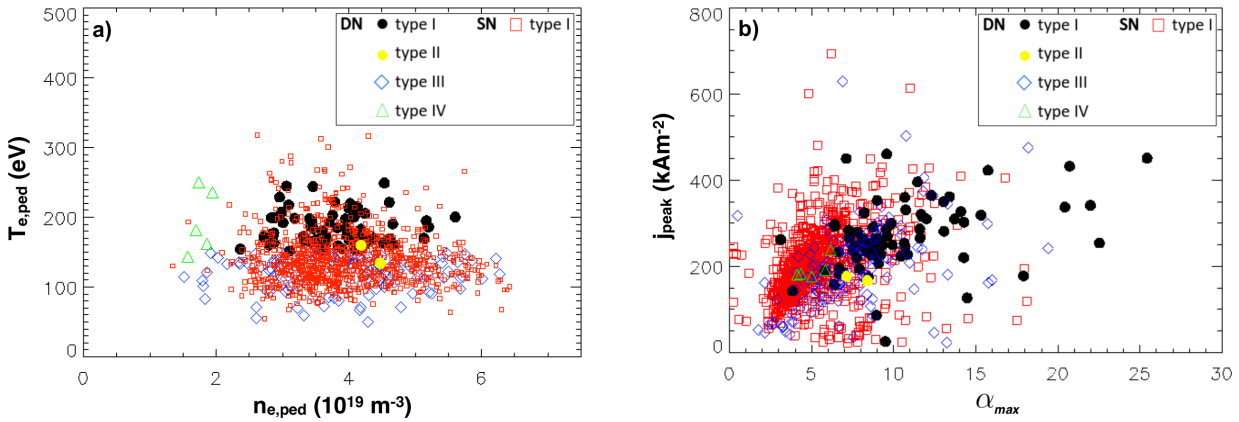

Figure 3: *a) Temperature pedestal height as a function of the density pedestal height. b) The peak parallel current density as a function of maximum pressure gradient for the different ELM types.*

pressure gradients, relative to the other ELMs. The type IV ELMs are located at slightly increased j_{peak} and lower pressure gradients in comparison to the type III ELMs. The results are consistent with previous MAST experimental data analysis in [11, 34].

Fig. 4 shows various pedestal quantities as a function of the pedestal collisionality (ν_e^*). Here $\nu_e^* = 6.92 \times 10^{-18}\, R\, q_{95}\, n_{e,ped}\, \ln\Lambda_e / (T_{e,ped}^2\, \epsilon^{3/2})$, where $\ln\Lambda_e = 31.3 - \ln(\sqrt{n_{e,ped}}/T_{e,ped})$ and ϵ is the inverse aspect ratio. The type I ELM profiles in the SN configuration cover a large range of collisionalities. The pedestal collisionality does not exceed 2 for the type I ELMs in DN. Type III ELMs are at higher collisionalities, rarely below $\nu_e^* \sim 0.7$, unlike the type IV ELMs that are at a lower collisionality and rarely exceed $\nu_e^* \sim 0.7$. The type II ELM characteristics are discussed in section 5.

The normalised pressure gradient is plotted as a function of the pedestal collisionality in fig. 4a), in general α_{max} decreases with increasing ν_e^* for the type I and III ELMs. The range of α_{max} for the type III ELMs appears to overlap with type I α_{max} values. The type IV ELMs are located at both low α_{max} and ν_e^*. The normalised pedestal poloidal pressure $\beta_{\theta,ped}$ is shown as a function of the collisionality in fig. 4b), where the pedestal poloidal beta is calculated using $\beta_{\theta,ped} = 2\mu_0 p_{ped}/B_\theta^2$, as in [35, 36]. Where the averaged poloidal magnetic field at the pedestal top $B_\theta = \mu_0 I_p / L_p$ and L_p is the circumference of the last closed flux surface. A trend of decreasing $\beta_{\theta,ped}$ with increasing ν_e^* is indicated. The type I ELM regimes reach higher $\beta_{\theta,ped} \leq 0.5$ values than the other ELM types. The type III ELMs reach a limit of around $\beta_{\theta,ped} \sim 0.25$ and the type IV ELMs a limit of $\beta_{\theta,ped} \sim 0.15$.

Throughout the ELM cycle, the pedestal energy is higher for type I ELM regimes in DN compared to the SN configuration, where $W_{ped,SN} \sim 0.6 \times W_{ped,DN}$. This is mostly due to the increased plasma volume of the DN, where the volume is $\sim 30\%$ larger in comparison to the SN. The percentage of energy lost from the pedestal ($\Delta W/W_{ped}$) is calculated and shown in fig. 4c), as a function of ν_e^*. $\Delta W/W_{ped}$ is calculated as, $\Delta W/W_{ped} = \Delta n/n_{ped} +$

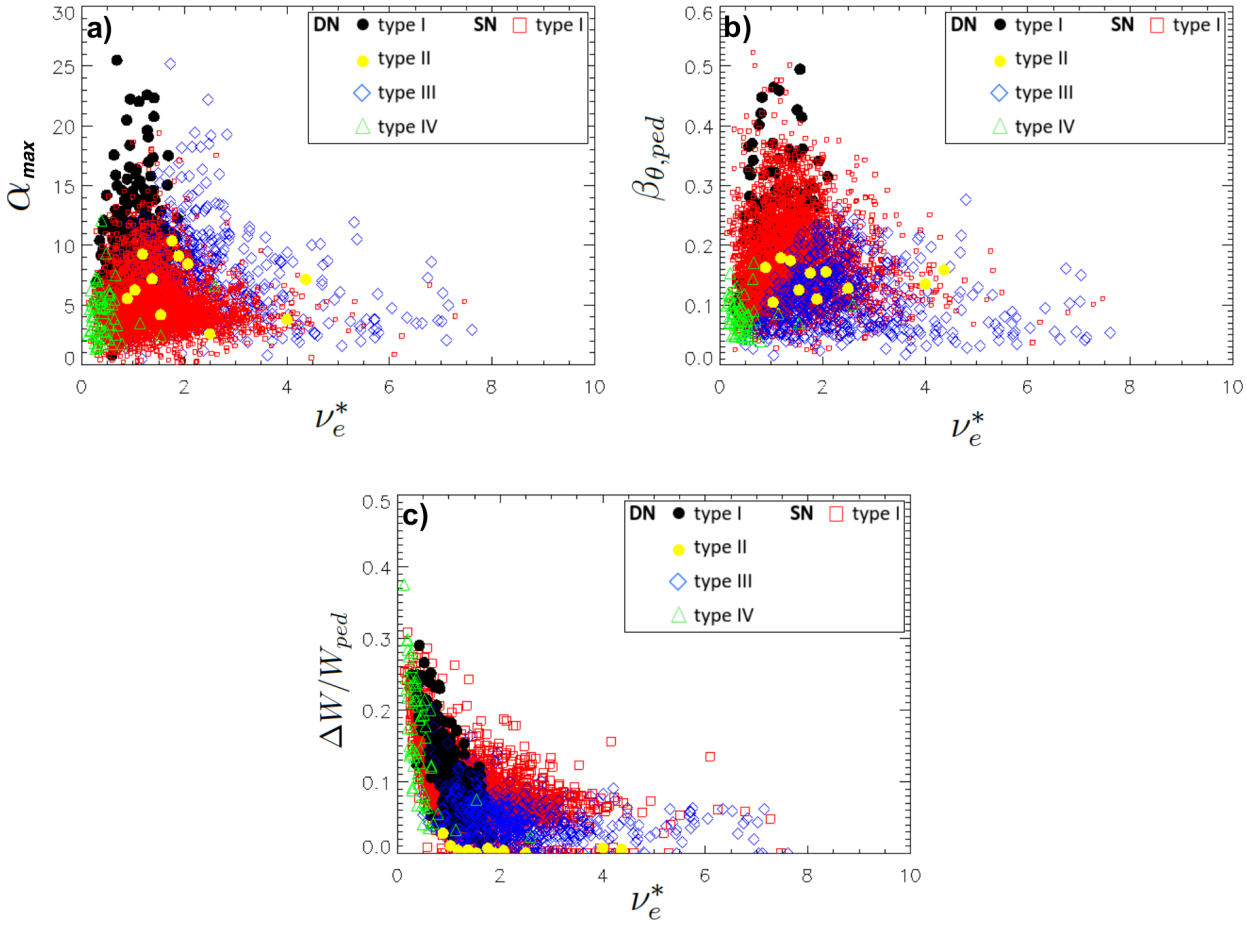

Figure 4: *a) The pressure gradient, b) the normalised pedestal poloidal pressure and c) the pedestal energy loss as a function of the collisionality for the different ELM regimes.*

$\Delta T/T_{ped}$, the first term describes the convective ELM energy losses and the second term the conductive losses. Higher pedestal energy losses are observed for all ELM types with decreasing collisionality. Up to $\Delta W/W_{ped} \sim 30\%$ measured for the type I and IV ELMs, with type III ELMs at lower $\Delta W/W_{ped}$ up to $\sim 12\%$. On average the type III ELMs have lower $\Delta W/W_{ped}$ than the type I ELMs, but there is an overlap in the pedestal energy losses.

3.2 HFS and LFS pedestal comparison

Determining how the density pedestal structure is formed is important for future tokamaks [37], by comparing the HFS and LFS pedestals the mechanism(s) (neutral fuelling versus transport) could be determined. Future pedestal predictive models could be informed by this, where the pedestal density could be eliminated as an input.

At MAST, it is possible to directly compare the HFS and LFS pedestal data from the TS diagnostic. In the MAST database, the SN shots are all fuelled from the LFS, and the DN shots are fuelled from the HFS, either at the mid-plane or at the upper and lower x-points. From the database, $T_{e,ped}$ and the pedestal electron temperature width (ΔT_e), in ψ-space

are found to be the same on the HFS and LFS. $n_{e,ped}$ is also the same at the inboard and outboard mid-plane. However, as seen previously on MAST [11] and shown in fig. 5a), the density pedestal width (Δn_e) varies on a flux surface, indicating density is not necessarily a flux surface quantity. Δn_e is in general narrower on the HFS than the LFS, for the DN configuration and to a lesser extent in the SN. The type III and IV ELM regimes appear to have an larger discrepancy in Δn_e, and ΔT_e appears to be narrower on the HFS, although more type III and type IV ELM data is needed to confirm this.

Comparing the HFS and LFS pedestals, in real space, it is observed that ΔT_e is wider on the HFS. Δn_e is also wider on the HFS, especially for SN configurations as shown in fig. 5b). It is suggested in [37] that density pedestal structure is strongly influenced by neutral fuelling but transport effects should not be neglected. The MAST data shows a better correlation for the DN in real space and poor correlation in ψ-space suggesting that here neutral fuelling plays an important role in the pedestal structure. The neutrals do not interact with the magnetic field, so if the pedestal width is determined by neutrals then changes in length scales will depend on plasma parameters in real space and be independent of magnetic geometry and flux surfaces. The opposite is found for the SN configuration, where a stronger correlation is found in ψ-space between the HFS and LFS pedestal widths.

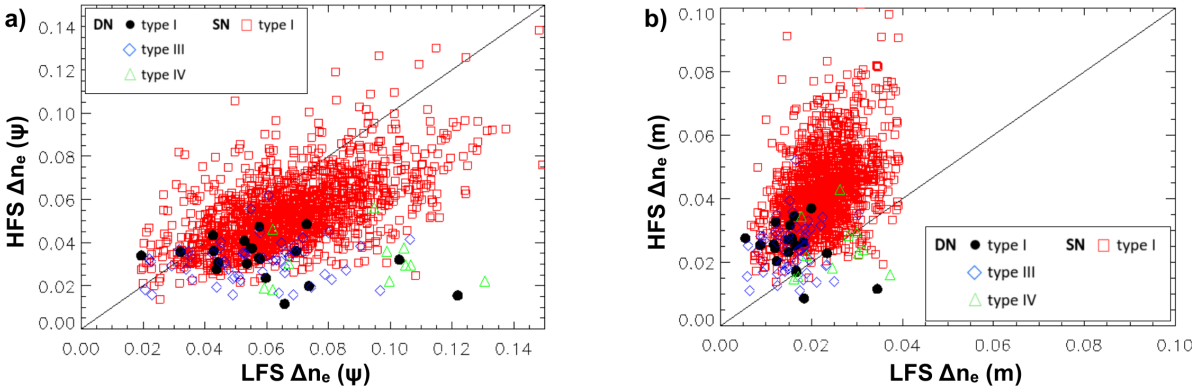

Figure 5: *The pedestal density width on the inboard side versus the pedestal density width on the outboard side in a) ψ-space and b) in real space.*

The edge current and pedestal pressure widths are also found to be are narrower on the HFS in ψ-space. The narrower inboard pedestal may have an effect on the stability. Currently, MHD codes calculate equilibria assuming flux surface quantities, which as shown here is not always the case. Simulations performed, using JOREK [38–40], are underway to investigate the impact of poloidal variation of density on the MHD stability. Initial studies show the growth rate of the low toroidal mode numbers (peeling modes) were affected, but the growth rate of the high-n (ballooning modes) were unaffected, due to their localisation at the outboard edge, where the pedestal is unchanged. However, further work is required to confirm if this is a physical effect [41], if confirmed a fully predictive pedestal model should

account for this, especially when considering equilibria that are unstable to low n modes.

3.3 Bootstrap current calculations and comparisons of analytical formulae

The bootstrap current (j_{BS}) usually dominates the current profile in the edge region. The Sauter formula is widely used for calculating the bootstrap current contribution to the current profile but has been found to over estimate the j_{BS} at high collisionality [42]. Recently, a new analytical formula for calculating the bootstrap current was found [14], here we refer to this as the "Redl" formula for the bootstrap current. The Redl formula was derived from the numerical code NEO [43, 44]. Here comparisons of the edge peak bootstrap current, calculated using the Redl and Sauter formulae for the MAST database, are shown in fig. 6, as a function of ν_e^*. The ratio $j_{BS,Redl}/j_{BS,Sauter}$ decreases with increasing ν_e^*, where there is good agreement around the medium to low range ν_e^*.

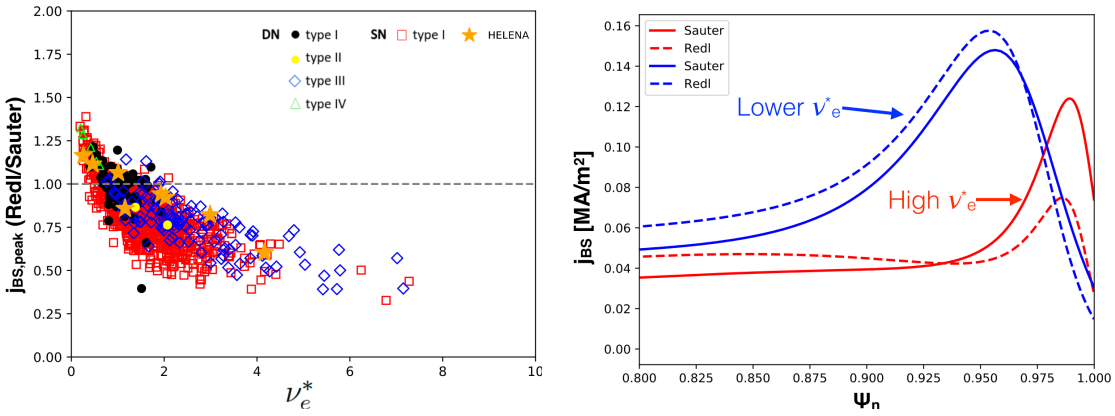

(a) (b)

Figure 6: *The ratio of the peak current density ($j_{BS,Redl}/j_{BS,Sauter}$) as a function of collisionality for the type I ELMs, where stars represent calculations from HELENA. b) Comparison of edge bootstrap current profiles calculated using the Sauter and Redl formulae. A MAST pedestal with lower collisionality $\nu_e^* = 1.0$ given in blue and a high collisionality pedestal with $\nu_e^* = 4.2$ given in red.*

The Redl formula has also been implemented in HELENA [15] equilibrium calculations. Several type I ELMy regime shots, in SN and DN configurations, at a range of ν_e^* have been input to HELENA to compare the two models, as seen in fig. 6, given by the orange stars. From the HELENA calculations, the cases with best and worst agreement of $j_{BS,peak}$ for MAST pedestals with lower $\nu_e^* = 1.0$ and at high $\nu_e^* = 4.2$ respectively are chosen. The edge bootstrap current profiles from these HELENA calculations are shown in fig. 6b). The two calculations agree reasonably well for low collisionality but at high collisionality the Sauter calculation is significantly increased in the pedestal, as the separatrix region is approached, in comparison to the Redl calculation. A next step, to validate the Redl formula for MAST

would be to compare the Redl formula implemented in HELENA with NEO for a range of ν_e^*.

4 MAST ELM data for Europed inputs

In this section we aim to validate the assumptions of Europed using the MAST data. The Europed code is based on the EPED1 model, and is currently being used and developed in an attempt to make consistent pedestal predictions. This knowledge can be used to inform spherical tokamak pedestal research, it will be important to accurately predict the pedestal in these future machines, to determine the P-B pedestal limits and avoid large ELM regimes. The experimental data in this section is from the last 25% of the ELM cycle. Only type I ELMs are analysed, in both SN and DN, as currently there is no model within Europed that can be used for predictions of pedestals for other ELM types.

Plasma parameters are given as inputs to Europed including global parameters B_T and I_p, the plasma boundary or shaping parameters, $n_{e,ped}$, separatrix density ($n_{e,sep}$), the profile shapes in the core for the density and temperature, as well as the total plasma β and the effective charge Z_{eff}. Most of these parameters can be determined ahead of experiments, but it is much more complex to predict $n_{e,ped}$, $n_{e,sep}$ and Z_{eff}. There is ongoing work, which attempts to eliminate the density pedestal parameters as inputs [16, 41].

When a Europed prediction is performed, a range of pedestal widths are defined, for each pedestal width the equilibrium is solved for in HELENA, before the code tests the ideal MHD stability over a range of toroidal mode numbers (n=1,2,3,4,5,10,20,30,50,70). Here, the ideal MHD code MISHKA [45, 46] is used for the stability calculations. Using the stability results and stability criterion, $\gamma = \gamma_{\text{crit}} = \omega^*/2$, where ω^* is the average diamagnetic frequency defined as half of the maximum diamagnetic frequency in the pedestal region, the code finds the pedestal stability limit, which corresponds to a predicted pedestal profile that is marginally stable.

The model assumes 1) a scaling for the pedestal width, that has been observed on multiple devices. This scaling is heuristically justified on the basis of kinetic ballooning modes (KBMs), providing a constraint on the maximum pedestal width. Where a relationship between the normalised poloidal pedestal pressure ($\beta_{\theta,ped}$) and the pressure pedestal width (Δp_e) is defined as $\Delta p_e = C\sqrt{\beta_{\theta,ped}}$. Where C is the width constant and can be determined from fits to experimental data. 2) The pedestal should be peeling-ballooning limited. The P-B stability is evaluated, using a range of toroidal mode numbers, in Europed the stability calculation then provides a constraint on the maximum pedestal height. From these assumptions, 1) and 2), a prediction can be made for the pedestal height and width. It is also assumed in Europed that the temperature and density pedestal widths are equivalent

($\Delta T_e = \Delta n_e$) and the ion and electron temperatures are assumed to be the same ($T_i = T_e$).

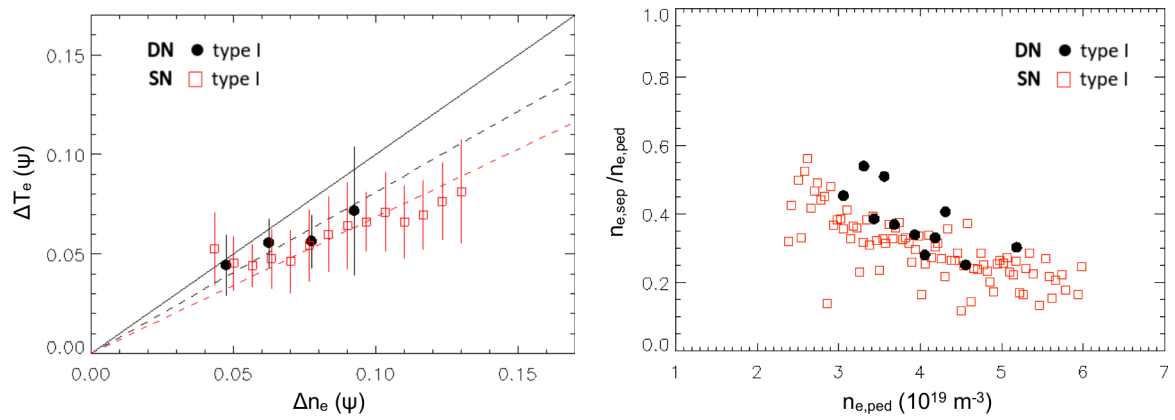

(a) (b)

Figure 7: *a) The temperature pedestal width versus the density pedestal width in ψ-space, the dashed lines indicate fits to the binned data. b) The ratio of the separatrix density to the pedestal density as a function of the pedestal density.*

As previously mentioned, for MAST plasmas, comparisons of T_i profiles from CXRS and T_e profiles from the TS system were performed in [29, 30]. It was found that $T_i = T_e$ is valid for certain collisionalities and is in general valid at the pedestal top.

Originally, in Europed, the density and temperature pedestal widths are assumed equal, and used to determine the pressure pedestal width. This is not necessarily the case for MAST pedestals, as shown in fig. 7a). In the SN configuration $\Delta T_e \sim 0.68 \pm 0.05 \Delta n_e$ and $\Delta T_e \sim 0.81 \pm 0.11 \Delta n_e$ for the DN configuration. Europed now has the functionality to specify this ratio [41]. Using the pedestal width ratio requires more prior knowledge, two more inputs of two known quantities from experiment. A test has been performed with two MAST cases, a SN and a DN case. The width ratio was specified using the values found from the experimental database given above. By including the width ratio a less than 3% change in the pedestal height and a less than 2% change in the pedestal width was found. As this is a minor difference and requires more experimental inputs, the assumption that $\Delta n_e = \Delta T_e$ will be used in the following Europed predictions in this paper.

There is an assumption that the separatrix density is some factor (f) of the pedestal density height, where $n_{e,sep} = f \times n_{e,ped}$. Fig. 7b) of the MAST experimental pedestal data indicates f decreases with increasing pedestal density height. When binned and the weighted mean calculated the separatrix density data, calculated at the location where $T_{e,sep} = 40$ eV [47, 48], is reasonably constant across all the MAST shots for the range of pedestal densities. The effect, on the pedestal prediction, of the changing separatrix density is minimal on tokamaks such as JET, where previously a scan of f (ie. $n_{e,sep}$) was performed [16] over a range (f=0.1-0.4). Varying f from 0.1 to 0.6, for a SN and a DN MAST case, results in the

predicted value of the pedestal temperature height and width changing by less than $\sim 25\%$ and $\sim 18\%$ respectively.

The relative positions of the density ($n_{e,pos}$) and temperature ($T_{e,pos}$) pedestals have been analysed and, in general, it is found that ($n_{e,pos}$) is shifted radially outwards of ($T_{e,pos}$). In JET ITER-like-wall (JET-ILW) it has been shown that this resulting finite relative shift directly impacts Europed predictions of the pedestal [49, 50]. Furthermore, an increased relative shift results in a flattening of the density pedestal radially inward of the separatrix. This leads to a reduction in the normalised density gradient $\nabla n_e/n_e$ and therefore an increase in the parameter $\eta_e \propto (\nabla n_e/n_e)^{-1}$. This in turn can lead to more virulent electron temperature gradient (ETG) microinstabilities and therefore increased levels of turbulent heat transport [51–53]. The role of the relative shift on both turbulent heat transport and Europed predictions in MAST is therefore something that should be verified in future work.

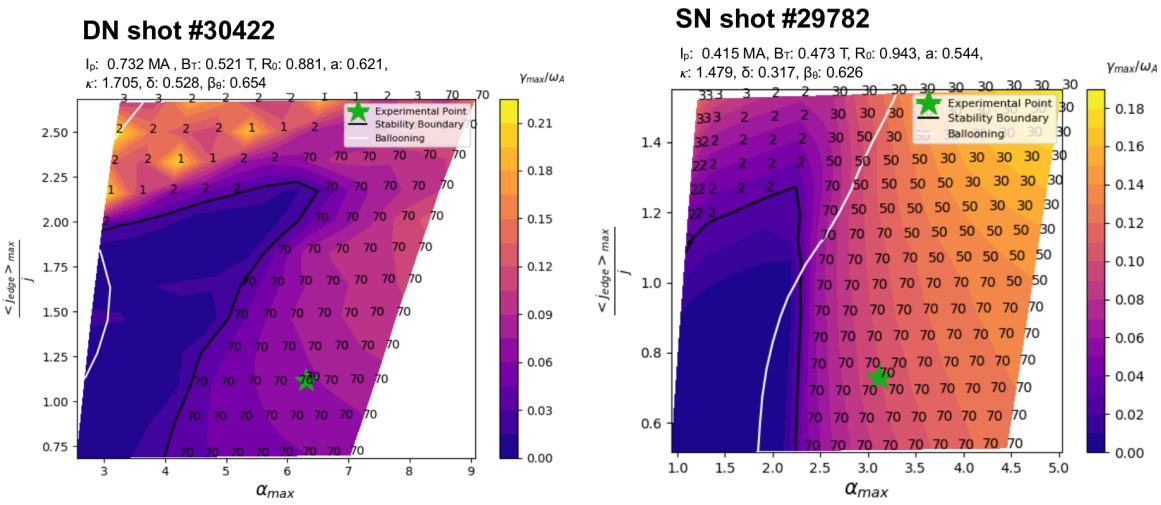

(a) (b)

Figure 8: *The stability plots for a double null (shot #30422) a) and a single null (shot #29782) b) discharge.*

If experimental data is available, it is possible to verify if a particular case is close to the P-B stability boundary giving an indication of whether the Europed prediction will be reasonable, where the pedestal should be limited by P-B modes. ESSIVE is used to check the stability, it uses HELENA to generate equilibria within a range of j and α space. MISHKA is then used to test the MHD stability of each equilibrium, over a range of toroidal mode numbers (n=1,2,3,4,5,10,20,30,50,70). P-B diagrams are shown in fig. 8a) and 8b) for examples of a MAST DN and SN configuration respectively. These shots were chosen as they cover a large range of MAST global and shaping parameter space. The DN and SN global and shaping parameters are given in fig. 8a) and 8b) respectively. These shots also have long periods of type I ELMs with a high amount (for MAST) of ELM cycles, such that

ELM averaged profiles can be used. In both configurations the experimental point is located in the unstable region close to the ballooning boundary, consistent with [19]. Note that not all MAST type I ELMs are in this unstable region.

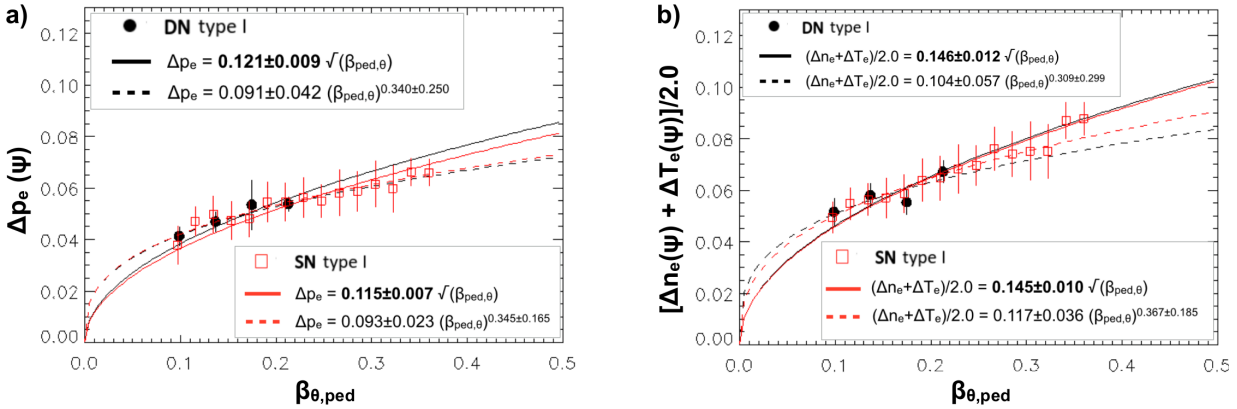

Figure 9: *a) The pressure pedestal width as a function of the pedestal normalised poloidal pressure. b) The pressure width averaged from the density and temperature pedestal widths as a function of* $\beta_{\theta,ped}$.

The MAST data is used to determine if the KBM constraint on the pedestal width, $\Delta p_e = C\sqrt{\beta_{\theta,ped}}$, is a good approximation for MAST. Δp_e is shown as a function of $\beta_{\theta,ped}$, in fig. 9 for the type I ELM regimes in the SN and DN configurations. In Europed $\Delta p_e = (\Delta n_e + \Delta T_e)/2.0$ is used. As shown by comparing fig. 9a) with fig. 9b) the two are not equivalent in MAST. From the pedestal database it is found that $\Delta p_e \sim 0.8 \times (\Delta n_e + \Delta T_e)/2.0$, therefore, the pressure width for MAST could be incorrectly predicted by Europed. In fig. 9 the solid lines indicate the linear fit to $\sqrt{\beta_{\theta,ped}}$, where a value for C is given in the figure. The dashed lines show the fit to the data, where the $\Delta = C(\beta_{\theta,ped})^b$, both C and the exponent b decrease in the fit. The values of C and b are also given in fig. 9. The value of b is consistent with 0.5 within the errors, and the fit to $\sqrt{\beta_{\theta,ped}}$ is reasonable, so the constraint could be valid for the MAST pedestal predictions, with the correct choice of C.

A test is performed in Europed where C is scanned, the predicted pedestal height and width can then be compared to the experimental values. This was done for MAST shots #29782 (SN) and #30422 (DN). The averaged profiles from the last 25% of the ELM cycle are used from the type I ELMy period. Fig. 10 shows the results of the width constant scan. As C is increased both the pedestal height and width increase. The dashed line indicates agreement between the Europed prediction and the experimental value, the prediction agrees with the experimental values at different C for the pedestal height and width. The temperature pedestal height is correctly predicted at $C \sim$0.13 for the DN case and $C \sim 0.145$, for the SN. This is also the case for the pedestal pressure.

The temperature pedestal height is predicted to within 10% for the value of C calculated

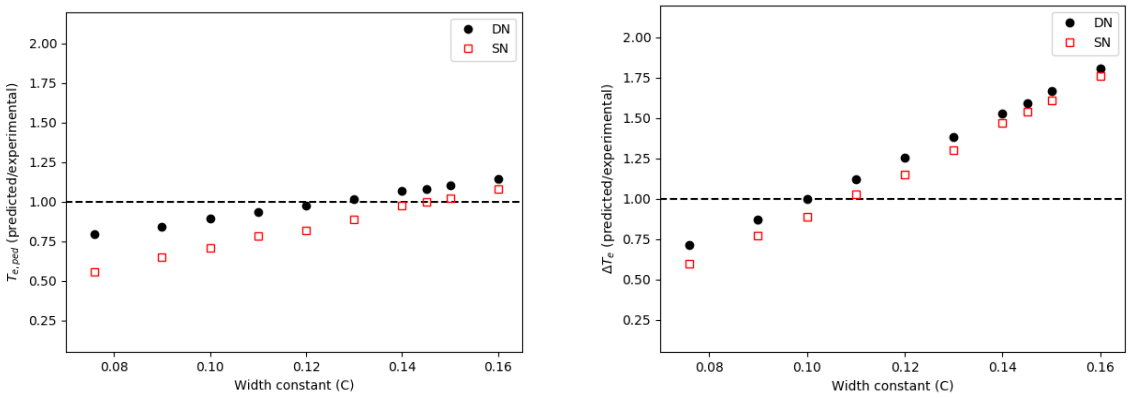

(a) (b)

Figure 10: *A scan in C for a SN and a DN case showing a) the pedestal temperature height and b) the pedestal temperature width. The predicted values are normalised to the experimental value, where the dashed black line indicates agreement.*

from the linear fit to the experimental data, when $\Delta p_{e,av}$ is used (fig. 9b)), for both cases. However, the pedestal width is overestimated for the same value of C, the correct pedestal width is predicted at a lower value of C$\sim$0.10-0.11. The double null pedestal height and width is predicted at lower values of the width constant in comparison to the single null configuration.

The choice of the width constant is important as this can have a significant effect on the pedestal prediction, this should be kept in mind when attempting to make reliable pedestal predictions for spherical tokamaks, such as MAST-U and beyond toward tokamaks such as STEP.

5 Type II ELM regimes and stability analysis

A potential H-mode regime for future spherical tokamaks, such as STEP, could be a type II ELM regime and research is underway to investigate this. Type II ELMs are small, releasing less pedestal energy during an event and thus lower heat fluxes reach divertor targets. Here, type II ELMs from the MAST pedestal database are analysed. Ideal MHD stability analysis and parameter scans are performed using ESSIVE, where comparisons between type I and type II ELMs are made.

Type II ELM regimes in MAST [20] have only been observed in DN, where the plasma is highly shaped. Comparisons have previously been made for type II ELMs in MAST plasmas to other tokamaks, such as NSXT [24] and ASDEX Upgrade [20], where similar characteristics have been identified on each device. In MAST, one difference to the ASDEX Upgrade type II regime, is that the type II ELM filaments have low density, this results

in low density transport. The pedestal can then evolve and trigger a type I ELM. MAST type II ELM regimes are interspersed with type I ELMs, whereas at ASDEX Upgrade [20], the higher density pump out can allow for a sustained type II ELM regime. It has been suggested that the type II ELMs at ASDEX Upgrade might be ballooning modes, which are localised close to the separatrix [22]. Here, stability analysis is performed for type II ELMs on MAST.

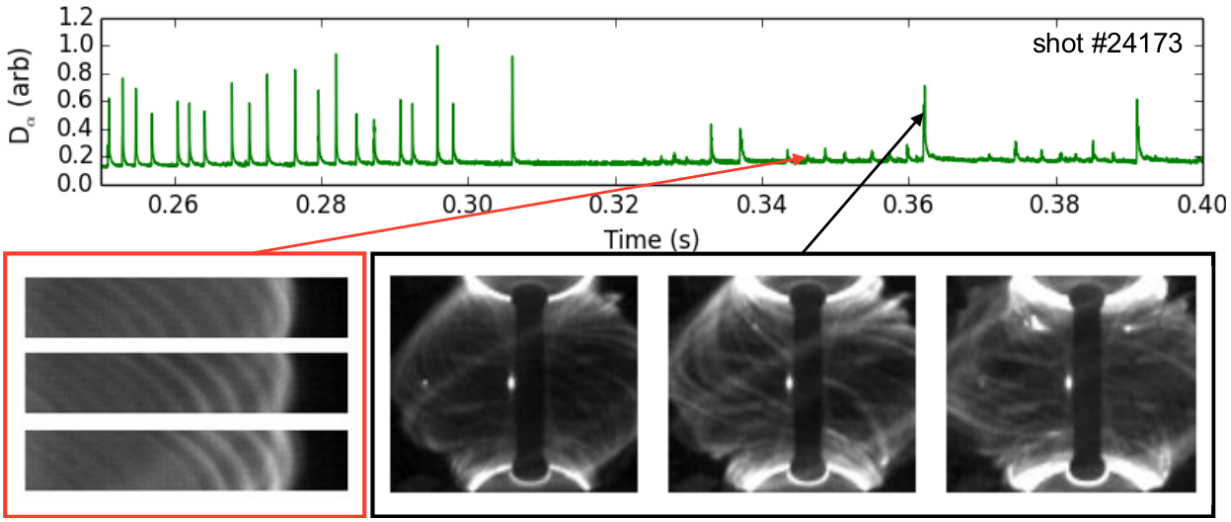

Figure 11: *The D_α trace for shot #24173 given above with fast camera frames, focused at the plasma edge, during the small ELM at t=346 ms (within the red outline on the left), and images during the type I ELM at t=363 ms (within the black outline).*

5.1 Analysis of type II experimental data

In general the type II ELM filaments are thought to originate closer to the LCFS, with lower toroidal and radial velocities, and do not appear to detach. The type II ELMs have the highest toroidal mode number (n) compared to other ELM types, where $n \sim$ 20-30, indicating more of a ballooning mode [20]. In fig. 11 fast camera images are shown for a type I and a type II ELM, where the ELMs are indicted on the D_α trace. The small ELMs appear as small peaks on the D_α trace (a zoom of the D_α trace from fig. 1g)) where as the larger peaks indicate type I ELMs. The fast camera shows uniform and numerous filaments for the type II ELMs, whereas nonlinear and fewer larger filaments are observed during the type I ELMs.

Type II ELMs occur at higher collisionality in MAST, $\nu_e^* \geqslant 1$, as shown in figs. 4a)-c). This limit is consistent with previous observations in [24]. Fig. 4b) shows an upper limit of ~ 0.2 for $\beta_{\theta,ped}$ for the type II ELMs, a limit of $\beta_{ped} \sim 0.05$ is also found. Again, the results are consistent with previous findings [20, 24], and at larger pedestal β type I ELMs occur.

Pedestal energy losses are consistently lower for the type II ELMs, compared to the other ELM types, where $\Delta W/W_{ped} < 3\%$, as shown in fig. 4c). During the type II ELM crash $T_{e,ped}$ remains constant so only the convective part of ΔW is calculated here.

The type II ELM regimes can cover a range of pedestal heights. Where $T_{e,ped}$ is mostly between the type I and type III ELMs in DN. $n_{e,ped}$ in a type II regime is similar to that for the type I. Fig. 3 shows only 2 data points for the type II ELMs in the final 25% of the ELM cycle, due to lack of data it is difficult to draw conclusions but it appears that the type II ELMs (yellow circles Fig. 3 b)) are positioned at lower j_{peak} and α_{max} relative to the type I ELMs in DN configuration (black circles).

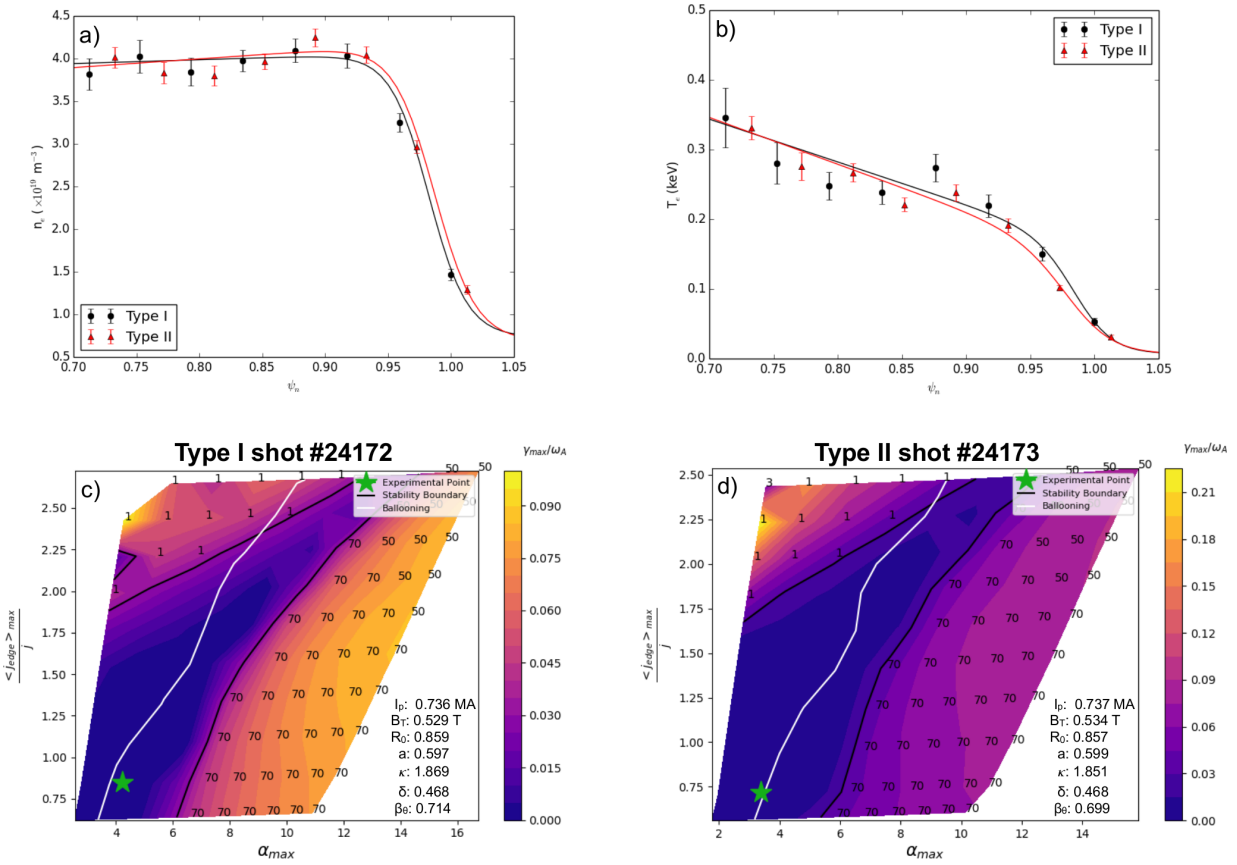

Figure 12: *a) Temperature and b) density profiles prior to a type I and type II ELM. Stability plots for c) type I and d) type II ELMs, produced using ESSIVE. The green star represents the experimental point, the solid black line indicates the stability boundary and the white line shows the infinite n ballooning boundary.*

5.2 Ideal MHD stability analysis of type II ELMs

Ideal MHD stability analysis of the type II ELMs indicates whether the pedestal is located close to the peeling-ballooning boundary. The profiles just before a type I ELM from shot #24172 and a type II ELM from shot #24173 are input into ESSIVE to investigate P-B

stability. Shot #24173 is a repeat of #24172, these shots have very similar global and shaping parameters, and are given in fig. 12. The D_α traces for each shot shows type II ELM regimes interspersed with type I ELMs.

The electron temperature and density profiles are for a single TS time point taken from the last 25% of the ELM cycle, shown in fig. 12a) and 12b). It was not possible to use time averaged profiles for the analysis due to lack of data at the end of the ELM cycles, in the type II ELM shots. The type I and type II profiles are similar, with very little difference between the pedestal profiles. Again, ESSIVE is used to investigate the ideal MHD stability, over a range of toroidal mode numbers (n=1,2,3,4,5,10,20,30,50,70).

The stability plots for the type I and II ELMs are shown in fig. 12c) and 12d) respectively. As expected due to the similarities in the input profiles the stability diagrams are alike. The type II ELM experimental point is located at a lower j_{peak} and α_{max}, compared the type I ELM. Both the type I and II pedestals are in the stable region of the P-B stability diagram. The type II is also stable in the pedestal, in contrast to the type I ELM, which is locally marginally unstable to $n = \infty$ ballooning modes at around $\psi_n = 0.963 - 0.975$. As shown in fig. 13a), comparing the type II (cyan dashed line) and the type I (blue solid line) ELMs. There is not much to distinguish the type I and the type II ELM cases shown here. The same result, in relation to ideal MHD stability, has been found for the only other type II ELM, from this MAST database, for which there was TS data in the last 25% of the ELM cycle. The stable region is extended at the P-B nose in the stability plot. A test has been performed, in this region, with increased poloidal resolution and also using ELITE for the stability analysis, in each case this region remained stable.

In most MAST type I regimes, that are not mixed with type II ELMs, the experimental point is positioned on or close to the ballooning boundary [19]. As shown in section 4, the type I pedestal experimental point is usually at a lower current density than the peeling-ballooning nose and is usually ballooning unstable. From fig. 13a) it is shown that, the pure type I ELM regimes, from section 4 in the SN (dotted magenta line) and DN (black solid line) configurations, are marginally unstable to $n = \infty$ ballooning modes across the pedestal. Especially, in comparison to the mixed type I and type II regimes, which are close to the stability boundary. In the future it would be interesting to investigate if this is the case for other spherical tokamaks by exploring type II ELMs in MAST-U and NSTX. Shot #30422 has similar global and shaping parameters as the type II shots, the most significant difference is the input power for the pure type I ELM regime, which is over double that of the type I/II mixed regimes. This is consistent with the power scan given in [20], where as the input power is increased the type II ELMs disappear and type I ELM regime is established. The fits to the TS profile data, which are input to ESSIVE, indicate the T_e, n_e and p_e pedestal

gradients are increased in shot #30422, in comparison to the type I and II profiles from the mixed regimes, resulting in the differences observed in the stability plots.

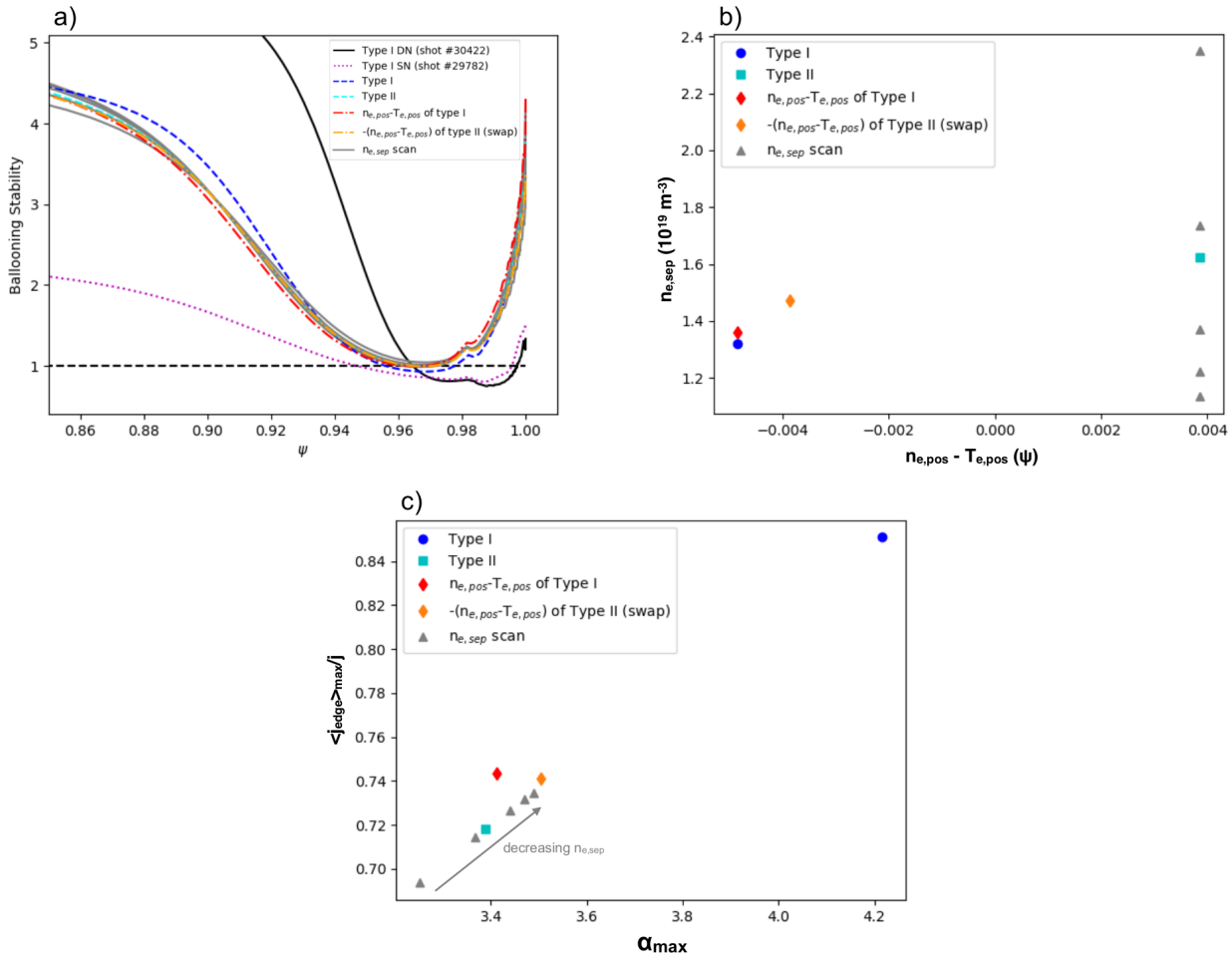

Figure 13: *a) The ballooning stability for the parameter scans. The horizontal black dashed line represents the ballooning stability threshold (below 1 is ballooning unstable). b) Values of* $n_{e,pos} - T_{e,pos}$ *and* $n_{e,sep}$ *for the type I and type II cases along with scans in the separatrix density and the relative pedestal position. c) The* $j - \alpha$ *values for the type I and II profiles and the scans in* $n_{e,pos} - T_{e,pos}$ *and* $n_{e,sep}$*.*

5.3 Effect of $n_{e,sep}$ and pedestal relative shift on stability

At ASDEX Upgrade, a higher separatrix density is observed during the type II ELM regime [20, 22]. A scan in the separatrix density is performed here, starting from the type II ELM case, to determine the effect on stability. Fig. 13b) indicates the range of separatrix densities (grey triangles), which are used in the scan. A wide range of separatrix densities have been scanned whilst the pedestal height remains fairly constant and the temperature profile remains unchanged. The values of j_{peak} and α_{max} are given in fig. 13c). Note that the axes in fig. 13c) are different to the $j - \alpha$ plots in fig. 12 and only small changes in the

pressure gradient and current density occur. As $n_{e,sep}$ is decreased j_{peak} and α_{max} increase. However, even at separatrix densities lower than the type I ELM case the higher type I values of j_{peak} and α_{max} are not reached. The $n_{e,ped}$ was decreased from the type II to the type I value, this resulted in a decrease in j_{peak} and α_{max}.

From the experimental profiles in fig. 12 a) and b) the relative shift $(n_{e,pos} - T_{e,pos})$ of the pedestal positions appears to be one of the differences between the type I and type II profiles. $n_{e,pos} - T_{e,pos}$ was varied, as shown in fig. 13b). First, the negative value of $n_{e,pos} - T_{e,pos}$ of the type II ELM is used to create new profiles for stability analysis. The orange diamonds in fig. 13 b) and c) represent this case. Using ESSIVE, the stability analysis indicates an increase in j_{peak} and α_{max}, when $n_{e,pos} - T_{e,pos}$ is decreased.

Then, $n_{e,pos} - T_{e,pos}$ is switched from the positive type II (cyan square) to the negative type I value (red diamond), note changing the relative shift also alters the separatrix density slightly. Using the new value for $n_{e,pos} - T_{e,pos}$ the density profile is very similar to that of the type I ELM profile in fig. 12a), but the temperature profile has a lower gradient, which results in a lower maximum pressure gradient. From the stability analysis, the decrease in $n_{e,pos} - T_{e,pos}$ again results in an increase in j_{peak} and α_{max}, comparing red diamond and cyan square in fig. 13c).

The ballooning stability calculation performed in HELENA indicates only small differences are observed in the pedestal region from the scans, as shown in fig. 13a). For the negative relative shift and the 3 lowest separatrix density cases the pedestal is only just locally ballooning unstable, at around $0.963 < \psi < 0.973$. As the separatrix density is decreased the pedestal region becomes more ballooning unstable. No single pedestal parameter, which has been explored here, with the ideal MHD code, is alone responsible for the difference between the type I and type II ELMs. To confirm these results, they should be repeated for more type II ELMs, here we have focused on one specific profile.

6 Conclusions

In summary, the MAST pedestal data from the new upgraded TS system used in the final 3 campaigns on MAST, is presented, allowing for an overview of pedestal characteristics. Trends in the different ELM types have been discussed and pedestal characteristics are consistent with previous MAST pedestal results in [11]. Direct comparisons of the HFS and LFS pedestal data was performed, made possible by the TS diagnostic, which has a view across the whole plasma at the mid-plane. The density appears to vary on a flux surface, where the pedestal width is, in general, narrower on the HFS. This should be considered when performing density pedestal predictions, especially if the MHD stability is affected. Bootstrap current calculations for the MAST database have been obtained and comparisons

of the Sauter and Redl formulae are performed. The two calculations agree at low ν_e^*, but deviate at higher ν_e^*, and the HELENA calculations also indicate this.

The assumptions for Europed have been tested with MAST data in anticipation of future spherical tokamak pedestal predictions. Most Europed assumptions hold including the KBM constraint on the pedestal width, where the value of the width constant was evaluated from the MAST database. It was found that $C \sim 0.145$ for MAST, this is almost twice that of previous studies on conventional tokamaks, where C=0.076 is obtained [17]. Using the attained value, $C \sim 0.145$, first MAST pedestal predictions were performed. The temperature pedestal height was predicted to within 10% for a SN and a DN shot. The pedestal height can be closely predicted using the width constant determined by experimental data, but the pedestal width is overestimated for the same value of C. This will be further confirmed with more MAST cases in future work.

Analysis of the MAST type II ELMs is performed. The stability analysis is performed with ESSIVE and indicates that both the type I and II ELMs in the mixed regimes have similar MHD stability properties, and are therefore difficult to distinguish using ideal MHD alone. Both are P-B stable unlike the type I ELM from a purely type I regime, which is located in the ballooning region of the stability diagram. Parameter scans of decreasing $n_{e,sep}$ and $n_{e,pos} - T_{e,pos}$ resulted in an increase in the maximum edge current density and pedestal pressure gradient. No threshold to a type I ELM was observed when individually varying these parameters.

The MAST pedestal data has been analysed here, similar pedestal characteristics have been found in a comparison to previous MAST pedestal data analysis. The data has been used to validate the Europed assumptions, where more confidence can be given to the Europed pedestal predictions. By predicting pedestals, which are limited by peeling-ballooning modes, large ELM regimes could be avoided in future tokamaks, where alternative operating regimes will be required. Future work could include confirming the results from the experimental database with data from machines, such as NSTX and MAST-U, to determine if the ELM features, which are observed here, are consistent with other spherical tokamaks. This will allow stronger conclusions to be drawn and the knowledge would contribute to future spherical tokamaks such as STEP.

7 Acknowledgement

This work has been carried out within the framework of the EUROfusion Consortium and has received funding from the Euratom research and training program 2014-2018 and 2019-2020 under Grant Agreement No. 633053. The views and opinions expressed herein do not necessarily reflect those of the European Commission.

References

[1] F. Wagner, G. Becker, K. Behringer, D. Campbell, A. Eberhagen, W. Engelhardt, G. Fussmann, O. Gehre, J. Gernhardt, G. v. Gierke, G. Haas, M. Huang, F. Karger, M. Keilhacker, O. Klüber, M. Kornherr, K. Lackner, G. Lisitano, G. G. Lister, H. M. Mayer, D. Meisel, E. R. Müller, H. Murmann, H. Niedermeyer, W. Poschenrieder, H. Rapp, H. Röhr, F. Schneider, G. Siller, E. Speth, A. Stäbler, K. H. Steuer, G. Venus, O. Vollmer, and Z. Yü. Regime of Improved Confinement and High Beta in Neutral-Beam-Heated Divertor Discharges of the ASDEX Tokamak. *Physical Review Letters*, 49(19):1408–1412, 11 1982. ISSN 0031-9007. doi: 10.1103/PhysRevLett.49.1408. URL https://link.aps.org/doi/10.1103/PhysRevLett.49.1408.

[2] A. Kirk, B. Koch, R. Scannell, H. R. Wilson, G. Counsell, J. Dowling, A. Herrmann, R. Martin, M. Walsh, and M. Walsh. Evolution of Filament Structures during Edge-Localized Modes in the MAST Tokamak. *Physical Review Letters*, 96(18):185001, 5 2006. ISSN 0031-9007. doi: 10.1103/PhysRevLett.96.185001. URL https://link.aps.org/doi/10.1103/PhysRevLett.96.185001.

[3] H Zohm. Edge localized modes (ELMs). *Plasma Physics and Controlled Fusion*, 38(2):105–128, 2 1996. ISSN 0741-3335. doi: 10.1088/0741-3335/38/2/001. URL http://stacks.iop.org/0741-3335/38/i=2/a=001?key=crossref.f28892e44e8eadadb5c7b755b5fc53e6.

[4] T. Eich, B. Sieglin, A.J. Thornton, M. Faitsch, A. Kirk, A. Herrmann, and W. Suttrop. ELM divertor peak energy fluence scaling to ITER with data from JET, MAST and ASDEX upgrade. *Nuclear Materials and Energy*, 12:84–90, 8 2017. ISSN 2352-1791. doi: 10.1016/J.NME.2017.04.014. URL https://www.sciencedirect.com/science/article/pii/S2352179116302927.

[5] E. Viezzer. Access and sustainment of naturally ELM-free and small-ELM regimes. *Nuclear Fusion*, 58(11):115002, 11 2018. ISSN 0029-5515. doi: 10.1088/1741-4326/aac222. URL https://iopscience.iop.org/article/10.1088/1741-4326/aac222.

[6] G. Fishpool, J. Canik, G. Cunningham, J. Harrison, I. Katramados, A. Kirk, M. Kovari, H. Meyer, and R. Scannell. MAST-upgrade divertor facility and assessing performance of long-legged divertors. *Journal of Nuclear Materials*, 438(SUPPL), 2013. ISSN 00223115. doi: 10.1016/j.jnucmat.2013.01.067.

[7] R. Scannell, M. J. Walsh, M. R. Dunstan, J. Figueiredo, G. Naylor, T. O'Gorman, S. Shibaev, K. J. Gibson, and H. Wilson. A 130 point Nd:YAG Thomson scattering diagnostic on MAST. *Review of Scientific Instruments*, 81(10):10D520, 10 2010. ISSN 0034-6748. doi: 10.1063/1.3460628. URL http://aip.scitation.org/doi/10.1063/1.3460628.

[8] Howard Wilson, Ian Chapman, Tris Denton, William Morris, Bhavin Patel, Garry Voss, Chris Waldon, and the STEP Team. STEP—on the pathway to fusion commercialization. In *Commercialising Fusion Energy*. IOP Publishing, 12 2020. doi: 10.1088/978-0-7503-2719-0ch8. URL https://iopscience.iop.org/book/978-0-7503-2719-0/chapter/bk978-0-7503-2719-0ch8.

[9] A Kirk, G F Counsell, H R Wilson, J-W Ahn, R Akers, E R Arends, J Dowling, R Martin, H Meyer, M Hole, M Price, P B Snyder, D Taylor, M J Walsh, Y Yang, and the MAST team. ELM characteristics in MAST. *Plasma Physics and Controlled Fusion*, 46(3):551–572, 3 2004. ISSN 0741-3335. doi: 10.1088/0741-3335/46/3/009. URL http://stacks.iop.org/0741-3335/46/i=3/a=009?key=crossref.67a666efd11ce548b75f650b25807b52.

[10] A Kirk, G F Counsell, E Arends, H Meyer, D Taylor, M Valovic, M Walsh, H Wilson, and the MAST team. H-mode pedestal characteristics on MAST. *Plasma Physics and Controlled Fusion*, 46(5A):A187–A194, 5 2004. ISSN 0741-3335. doi: 10.1088/0741-3335/46/5A/020. URL https://iopscience.iop.org/article/10.1088/0741-3335/46/5A/020.

[11] A Kirk, T O'Gorman, S Saarelma, R Scannell, and H R Wilson. A comparison of H-mode pedestal characteristics in MAST as a function of magnetic configuration and ELM type. *Plasma Physics and Controlled Fusion*, 51(6):065016, 6 2009. ISSN 0741-3335. doi: 10.1088/0741-3335/51/6/065016. URL https://iopscience.iop.org/article/10.1088/0741-3335/51/6/065016.

[12] A. Kirk, W. Suttrop, I.T. Chapman, Yueqiang Liu, R. Scannell, A.J. Thornton, L. Barrera Orte, P. Cahyna, T. Eich, R. Fischer, C. Fuchs, C. Ham, J.R. Harrison, M.W. Jakubowski, B. Kurzan, S. Pamela, M. Peterka, D. Ryan, S. Saarelma, B. Sieglin, M. Valovic, M. Willensdorfer, MAST, and ASDEX Upgrade Teams. Effect of resonant magnetic perturbations on low collisionality discharges in MAST and a comparison with ASDEX Upgrade. *Nuclear Fusion*, 55(4):043011, 4 2015. ISSN 0029-5515. doi: 10.1088/0029-5515/55/4/043011. URL http://stacks.iop.org/0029-5515/55/i=4/a=043011?key=crossref.d4c046c9f4286647dadfdc59a1a93799.

[13] O. Sauter, C. Angioni, and Y. R. Lin-Liu. Neoclassical conductivity and bootstrap current formulas for general axisymmetric equilibria and arbitrary collisionality regime.

Physics of Plasmas, 6(7):2834–2839, 7 1999. ISSN 1070-664X. doi: 10.1063/1.873240. URL http://aip.scitation.org/doi/10.1063/1.873240.

[14] A. Redl, C. Angioni, E. Belli, and O. Sauter. A new set of analytical formulae for the computation of the bootstrap current and the neoclassical conductivity in tokamaks. *Physics of Plasmas*, 28(2):022502, 2 2021. ISSN 1070-664X. doi: 10.1063/5.0012664. URL https://aip.scitation.org/doi/10.1063/5.0012664.

[15] G.T.A. Huysmans, J.P. Goedbloed, and W. Kerner. Isoparametric Bicubic Hermite Elements for Solution of the Grad-Shafranov Equation. *International Journal of Modern Physics C*, 02(01):371–376, 3 1991. doi: 10.1142/S0129183191000512. URL https://www.worldscientific.com/doi/abs/10.1142/S0129183191000512.

[16] S Saarelma, C D Challis, L Garzotti, L Frassinetti, C F Maggi, M Romanelli, and C Stokes. Integrated modelling of H-mode pedestal and confinement in JET-ILW. *Plasma Physics and Controlled Fusion*, 60(1):014042, 1 2018. ISSN 0741-3335. doi: 10.1088/1361-6587/aa8d45. URL https://iopscience.iop.org/article/10.1088/1361-6587/aa8d45.

[17] P. B. Snyder, R. J. Groebner, A. W. Leonard, T. H. Osborne, and H. R. Wilson. Development and validation of a predictive model for the pedestal height. *Physics of Plasmas*, 16(5):056118, 5 2009. ISSN 1070-664X. doi: 10.1063/1.3122146. URL http://aip.scitation.org/doi/10.1063/1.3122146.

[18] P.B. Snyder, R.J. Groebner, J.W. Hughes, T.H. Osborne, M. Beurskens, A.W. Leonard, H.R. Wilson, and X.Q. Xu. A first-principles predictive model of the pedestal height and width: development, testing and ITER optimization with the EPED model. *Nuclear Fusion*, 51(10):103016, 10 2011. ISSN 0029-5515. doi: 10.1088/0029-5515/51/10/103016. URL https://iopscience.iop.org/article/10.1088/0029-5515/51/10/103016.

[19] M. Knolker, T. Osborne, E. Belli, S. Henderson, A. Kirk, L. Kogan, S. Saarelma, and P.B. Snyder. Pedestal stability analysis on MAST in preparation for MAST-U. *Nuclear Fusion*, 61(4):046041, 4 2021. ISSN 0029-5515. doi: 10.1088/1741-4326/abe804. URL https://iopscience.iop.org/article/10.1088/1741-4326/abe804.

[20] A Kirk, H W Muller, E Wolfrum, H Meyer, A Herrmann, T Lunt, V Rohde, and P Tamain. Comparison of small edge-localized modes on MAST and ASDEX Upgrade. *Plasma Physics and Controlled Fusion*, 53(9):095008, 9 2011. ISSN 0741-3335. doi: 10.1088/0741-3335/53/9/095008. URL https://iopscience.iop.org/article/10.1088/0741-3335/53/9/095008.

[21] G Saibene, R Sartori, A Loarte, D J Campbell, P J Lomas, V Parail, K D Zastrow, Y Andrew, S Sharapov, A Korotkov, M Becoulet, G T A Huysmans, H R Koslowski, R Budny, G D Conway, J Stober, W Suttrop, A Kallenbach, M von Hellermann, and

M Beurskens. Improved performance of ELMy H-modes at high density by plasma shaping in JET. *Plasma Physics and Controlled Fusion*, 44(9):1769–1799, 9 2002. ISSN 0741-3335. doi: 10.1088/0741-3335/44/9/301. URL https://iopscience.iop.org/article/10.1088/0741-3335/44/9/301.

[22] G.F. Harrer, E. Wolfrum, M.G. Dunne, P. Manz, M. Cavedon, P.T. Lang, B. Kurzan, T. Eich, B. Labit, J. Stober, H. Meyer, M. Bernert, F.M. Laggner, and F. Aumayr. Parameter dependences of small edge localized modes (ELMs). *Nuclear Fusion*, 58 (11):112001, 11 2018. ISSN 0029-5515. doi: 10.1088/1741-4326/aad757. URL https://iopscience.iop.org/article/10.1088/1741-4326/aad757.

[23] J Stober, M Maraschek, G.D Conway, O Gruber, A Herrmann, A.C.C Sips, W Treutterer, H Zohm, and ASDEX Upgrade Team. Type II ELMy H modes on ASDEX Upgrade with good confinement at high density. *Nuclear Fusion*, 41(9):1123–1134, 9 2001. ISSN 0029-5515. doi: 10.1088/0029-5515/41/9/301. URL http://stacks.iop.org/0029-5515/41/i=9/a=301?key=crossref.ac5840ece94ca4abb44d263fe4a485d6.

[24] R. Maingi, A.E. Hubbard, H. Meyer, J.W. Hughes, A. Kirk, R. Maqueda, and J.L. Terry. Comparison of small ELM characteristics and regimes in Alcator C-Mod, MAST and NSTX. *Nuclear Fusion*, 51(6):063036, 6 2011. ISSN 0029-5515. doi: 10.1088/0029-5515/51/6/063036. URL https://iopscience.iop.org/article/10.1088/0029-5515/51/6/063036.

[25] R. Scannell, M. J. Walsh, P. G. Carolan, N. J. Conway, A. C. Darke, M. R. Dunstan, D. Hare, and S. L. Prunty. Enhanced edge Thomson scattering on MAST. *Review of Scientific Instruments*, 77(10):10E510, 10 2006. ISSN 0034-6748. doi: 10.1063/1.2237488. URL http://aip.scitation.org/doi/10.1063/1.2237488.

[26] M. J. Walsh, N. J. Conway, M. Dunstan, M. J. Forrest, and R. B. Huxford. Interactive optical design and realization of an optimized charge coupled device Thomson scattering system for the spherical tokamak START. *Review of Scientific Instruments*, 70(1):742–746, 1 1999. ISSN 0034-6748. doi: 10.1063/1.1149436. URL http://aip.scitation.org/doi/10.1063/1.1149436.

[27] E R ARENDS. *Density gradients in spherical tokamak plasmas*. PhD thesis, Technische Universiteit Eindhoven, 2003. URL https://doi.org/10.6100/IR564240.

[28] R. Scannell, M. Beurskens, P. G. Carolan, A. Kirk, M. Walsh, T. O'Gorman, and T. H. Osborne. Deconvolution of Thomson scattering temperature profiles. *Review of Scientific Instruments*, 82(5):053501, 5 2011. ISSN 0034-6748. doi: 10.1063/1.3581230. URL http://aip.scitation.org/doi/10.1063/1.3581230.

[29] Thomas Morgan. Measurement of MAST edge ion temperatures and velocities. 2011. URL https://etheses.whiterose.ac.uk/2098/?utm_term=wreo&utm_

source=twitterfeed&utm_medium=twitter#.YMCUwbEpqAk.mendeley.

[30] B. Lloyd, R.J. Akers, F. Alladio, S. Allan, L.C. Appel, M. Barnes, N.C. Barratt, N. Ben Ayed, B.N. Breizman, M. Cecconello, C.D. Challis, I.T. Chapman, D. Ciric, G. Colyer, J.W. Connor, N.J. Conway, M. Cox, S.C. Cowley, G. Cunningham, A. Darke, M. De Bock, E. Delchambre, G. De Temmerman, R.O. Dendy, P. Denner, M.D. Driscoll, B. Dudson, D. Dunai, M. Dunstan, S. Elmore, A.R. Field, G. Fishpool, S. Freethy, L. Garzotti, K.J. Gibson, M.P. Gryaznevich, W. Guttenfelder, J Harrison, R.J. Hastie, N.C. Hawkes, T.C. Hender, B. Hnat, D.F. Howell, M.-D. Hua, A. Hubbard, G. Huysmans, D. Keeling, Y.C. Kim, A. Kirk, Y. Liang, M.K. Lilley, M. Lisak, S. Lisgo, Y.Q. Liu, G.P. Maddison, R. Maingi, S.J. Manhood, R. Martin, G.J. McArdle, J. McCone, H. Meyer, C. Michael, S. Mordijck, T. Morgan, A.W. Morris, D.G. Muir, E. Nardon, G. Naylor, M.R. O'Brien, T. O'Gorman, J. Páleník, A. Patel, S.D. Pinches, M.N. Price, C.M. Roach, V. Rozhansky, S. Saarelma, S.A. Sabbagh, A. Saveliev, R. Scannell, S.E. Sharapov, V. Shevchenko, S. Shibaev, D. Stork, J. Storrs, W. Suttrop, A. Sykes, P. Tamain, D. Taylor, D. Temple, N. Thomas-Davies, A. Thornton, M.R. Turnyanskiy, M. Valovic, R.G.L. Vann, G. Voss, M.J. Walsh, S.E.V. Warder, H.R. Wilson, M. Windridge, M Wisse, and S. Zoletnik. Overview of physics results from MAST. *Nuclear Fusion*, 51(9):094013, 9 2011. ISSN 0029-5515. doi: 10.1088/0029-5515/51/9/094013. URL https://iopscience.iop.org/article/10.1088/0029-5515/51/9/094013.

[31] H R Wilson, J W Connor, A R Field, S J Fielding, R L Miller, L L Lao, J R Ferron, and A D Turnbull. Ideal magnetohydrodynamic stability of the tokamak high-confinement-mode edge region. *Physics of Plasmas*, 6:1925, 1999. doi: 10.1063/1.873492. URL https://doi.org/10.1063/1.873492.

[32] R. L. Miller, M. S. Chu, J. M. Greene, Y. R. Lin-Liu, and R. E. Waltz. Noncircular, finite aspect ratio, local equilibrium model. *Physics of Plasmas*, 5(4):973–978, 4 1998. ISSN 1070-664X. doi: 10.1063/1.872666. URL http://aip.scitation.org/doi/10.1063/1.872666.

[33] R Sartori, G Saibene, L D Horton, M Becoulet, R Budny, D Borba, A Chankin, G D Conway, G Cordey, D McDonald, K Guenther, M G von Hellermann, Yu Igithkanov, A Loarte, P J Lomas, O Pogutse, and J Rapp. Study of Type III ELMs in JET. *Plasma Physics and Controlled Fusion*, 46(5):723–750, 5 2004. ISSN 0741-3335. doi: 10.1088/0741-3335/46/5/002. URL http://stacks.iop.org/0741-3335/46/i=5/a=002?key=crossref.71688515a798c62fad8f1cb0db472b00.

[34] H. Meyer, R.J. Akers, F. Alladio, L.C. Appel, K.B. Axon, N. Ben Ayed, P. Boerner, R.J. Buttery, P.G. Carolan, D. Ciric, C.D. Challis, I.T. Chapman, G. Coyler, J.W. Connor, N.J. Conway, S. Cowley, M. Cox, G.F. Counsell, G. Cunningham, A. Darke,

M. deBock, G. deTemmerman, R.O. Dendy, J. Dowling, A. Yu Dnestrovskij, Yu.N. Dnestrovskij, B. Dudson, D. Dunai, M. Dunstan, A.R. Field, A. Foster, L. Garzotti, K. Gibson, M.P. Gryaznevich, W. Guttenfelder, N.C. Hawkes, J. Harrison, P. Helander, T.C. Hender, B. Hnat, M.J. Hole, D.F. Howell, M. Duc Hua, A. Hubbard, M. Istenic, N. Joiner, D. Keeling, A. Kirk, H.R. Koslowski, Y. Liang, M. Lilley, S. Lisgo, B. Lloyd, G.P. Maddison, R. Maingi, A. Mancuso, S.J. Manhood, R. Martin, G.J. McArdle, J. McCone, C. Michael, P. Micozzi, T. Morgan, A.W. Morris, D.G. Muir, E. Nardon, G. Naylor, M.R. O'Brien, T. O'Gorman, A. Patel, S.D. Pinches, J. Preinhaelter, M.N. Price, E. Rachlew, D. Reiter, C.M. Roach, V. Rozhansky, S. Saarelma, A. Saveliev, R. Scannell, S.E. Sharapov, V. Shevchenko, S. Shibaev, H. Smith, G.E. Staebler, D. Stork, J. Storrs, A. Sykes, S. Tallents, P. Tamain, D. Taylor, D. Temple, N. Thomas-Davies, A. Thornton, A. Thyagaraja, M.R. Turnyanskiy, J. Urban, M. Valovic, R.G.L. Vann, F. Volpe, G Voss, M.J. Walsh, S.E.V. Warder, R. Watkins, H.R. Wilson, M. Windridge, M. Wisse, A. Zabolotski, S. Zoletnik, and O. Zolotukhin. Overview of physics results from MAST. *Nuclear Fusion*, 49(10): 104017, 10 2009. ISSN 0029-5515. doi: 10.1088/0029-5515/49/10/104017. URL https://iopscience.iop.org/article/10.1088/0029-5515/49/10/104017.

[35] A. Diallo, R. Maingi, S. Kubota, A. Sontag, T. Osborne, M. Podestà, R.E. Bell, B.P. LeBlanc, J. Menard, and S. Sabbagh. Dynamical evolution of pedestal parameters in ELMy H-mode in the National Spherical Torus Experiment. *Nuclear Fusion*, 51 (10):103031, 10 2011. ISSN 0029-5515. doi: 10.1088/0029-5515/51/10/103031. URL https://iopscience.iop.org/article/10.1088/0029-5515/51/10/103031.

[36] R.J. Groebner, A.W. Leonard, P.B. Snyder, T.H. Osborne, C.F. Maggi, M.E. Fenstermacher, C.C. Petty, and L.W. Owen. Progress towards a predictive model for pedestal height in DIII-D. *Nuclear Fusion*, 49(8):085037, 8 2009. ISSN 0029-5515. doi: 10.1088/0029-5515/49/8/085037. URL https://iopscience.iop.org/article/10.1088/0029-5515/49/8/085037.

[37] S. Mordijck. Overview of density pedestal structure: role of fueling versus transport. *Nuclear Fusion*, 60(8):082006, 8 2020. ISSN 0029-5515. doi: 10.1088/1741-4326/ab8d04. URL https://iopscience.iop.org/article/10.1088/1741-4326/ab8d04.

[38] G.T.A Huysmans and O Czarny. MHD stability in X-point geometry: simulation of ELMs. *Nuclear Fusion*, 47(7):659–666, 7 2007. ISSN 0029-5515. doi: 10.1088/0029-5515/47/7/016. URL http://stacks.iop.org/0029-5515/47/i=7/a=016?key=crossref.54c4a396297481f3a5413a556faf8695.

[39] Olivier Czarny and Guido Huysmans. Bézier surfaces and finite elements for MHD simulations. *Journal of Computational Physics*, 227(16):7423–7445, 8 2008. ISSN 0021-9991.

doi: 10.1016/J.JCP.2008.04.001. URL https://www.sciencedirect.com/science/article/pii/S0021999108002118?via%3Dihub.

[40] Matthias Hoelzl, Guido Huijsmans, Stanislas Pamela, Marina Becoulet, Eric Nardon, Francisco Javier Artola, Boniface Nkonga, Calin Atanasiu, Vinodh Bandaru, Ashish Bhole, Daniele Bonfiglio, Andres Cathey, Olivier Czarny, Anastasiia Dvornova, Tamas Feher, Alexandre Fil, Emmanuel Franck, Shimpei Futatani, Marta Gruca, Herve Guillard, J Willem Haverkort, Ihor Holod, Di Hu, SangKyeun Kim, Sven Qurein Korving, Leon Kos, Isabel Krebs, Lukas Kripner, Guillaume Latu, Feng Liu, Peter Merkel, Dmytro Meshcheriakov, Verena Mitterauer, Serhiy Mochalskyy, Jorge Morales, Richard Nies, Nikita Nikulsin, Francois Orain, Dejan Penko, Jane Pratt, Rohan Ramasamy, Pierre Ramet, Cedric Reux, Konsta Särkimäki, Nina Schwarz, Prabal Singh Verma, Siobhan Faye Smith, Cristian Sommariva, Erika Strumberger, Daan van Vugt, Mark Verbeek, Egbert Westerhof, Fabian Wieschollek, and Jeffery Zielinski. The JOREK non-linear extended MHD code and applications to large-scale instabilities and their control in magnetically confined fusion plasmas. *Nuclear Fusion*, 4 2021. ISSN 0029-5515. doi: 10.1088/1741-4326/abf99f. URL https://iopscience.iop.org/article/10.1088/1741-4326/abf99f.

[41] C.J. Ham, A. Bokshi, D. Brunetti, G.Bustos Ramirez, B. Chapman, J.W. Connor, D. Dickinson, A.R. Field, L. Frassinetti, A. Gillgren, J.P. Graves, T.P. Kiviniemi, S. Leerink, B. McMillan, S. Newton, S. Pamela, C.M. Roach, S. Saarelma, J. Simpson, S.F. Smith, E.R. Solano, P. Strand, A.J. Virtanen, and the JET Contributors. Towards understanding reactor relevant tokamak pedestals. *Nuclear Fusion*, 61(9): 096013, 9 2021. ISSN 0029-5515. doi: 10.1088/1741-4326/ac12e9. URL https://iopscience.iop.org/article/10.1088/1741-4326/ac12e9.

[42] E A Belli, J Candy, O Meneghini, and T H Osborne. Limitations of bootstrap current models. *Plasma Physics and Controlled Fusion*, 56(4):045006, 4 2014. ISSN 0741-3335. doi: 10.1088/0741-3335/56/4/045006. URL https://iopscience.iop.org/article/10.1088/0741-3335/56/4/045006.

[43] E A Belli and J Candy. Kinetic calculation of neoclassical transport including self-consistent electron and impurity dynamics. *Plasma Physics and Controlled Fusion*, 50(9):095010, 9 2008. ISSN 0741-3335. doi: 10.1088/0741-3335/50/9/095010. URL https://iopscience.iop.org/article/10.1088/0741-3335/50/9/095010.

[44] E A Belli and J Candy. Full linearized Fokker–Planck collisions in neoclassical transport simulations. *Plasma Physics and Controlled Fusion*, 54(1):015015, 1 2012. ISSN 0741-3335. doi: 10.1088/0741-3335/54/1/015015. URL https://iopscience.iop.org/article/10.1088/0741-3335/54/1/015015.

[45] A.B. Mikhailovskii, G.T.A. Huysmans, W.O.K. Kerner, and S.E. Sharapov. Optimization of computational MHD normal-mode analysis for tokamaks. *Plasma Physics Reports*, 23(10):844–857, 1997. ISSN ISSN 1063-780X. doi: 10.1134/1.952514. URL https://inis.iaea.org/search/search.aspx?orig_q=RN:35015207.

[46] G T A Huysmans. ELMs: MHD instabilities at the transport barrier. *Plasma Physics and Controlled Fusion*, 47(12B):B165–B178, 12 2005. ISSN 0741-3335. doi: 10.1088/0741-3335/47/12B/S13. URL http://stacks.iop.org/0741-3335/47/i=12B/a=S13?key=crossref.63552efb26b61e44d10344002e7706b9.

[47] E Havlíčková, J Harrison, B Lipschultz, G Fishpool, A Kirk, A Thornton, M Wischmeier, S Elmore, and S Allan. SOLPS analysis of the MAST-U divertor with the effect of heating power and pumping on the access to detachment in the Super-x configuration. *Plasma Physics and Controlled Fusion*, 57(11):115001, 11 2015. ISSN 0741-3335. doi: 10.1088/0741-3335/57/11/115001. URL http://stacks.iop.org/0741-3335/57/i=11/a=115001?key=crossref.1189ca7b2936d4104038cb5efefc0dfb.

[48] A. Kallenbach, N. Asakura, A. Kirk, A. Korotkov, M. A. Mahdavi, D. Mossessian, and G. D. Porter. Multi-machine comparisons of H-mode separatrix densities and edge profile behaviour in the ITPA SOL and Divertor Physics Topical Group. In *Journal of Nuclear Materials*, volume 337-339, 2005. doi: 10.1016/j.jnucmat.2004.10.099.

[49] L. Frassinetti, M. G. Dunne, U. Sheikh, S. Saarelma, C. M. Roach, E. Stefanikova, C. Maggi, L. Horvath, S. Pamela, E. De La Luna, E. Wolfrum, M. Bernert, P. Blanchard, B. Labit, A. Merle, L. Guimarais, S. Coda, H. Meyer, and J. C. Hillesheim. Role of the pedestal position on the pedestal performance in AUG, JET-ILW and TCV and implications for ITER. *Nuclear Fusion*, 59(7), 2019. ISSN 17414326. doi: 10.1088/1741-4326/ab1eb9.

[50] E. Stefanikova, L. Frassinetti, S. Saarelma, C. Perez von Thun, J.C. Hillesheim, and JET contributors. Change in the pedestal stability between JET-C and JET-ILW low triangularity peeling-ballooning limited plasmas. *Nuclear Fusion*, 61(2):026008, 2 2021. ISSN 0029-5515. doi: 10.1088/1741-4326/abc838. URL https://iopscience.iop.org/article/10.1088/1741-4326/abc838.

[51] D. R. Hatch, M. Kotschenreuther, S. Mahajan, P. Valanju, and X. Liu. A gyrokinetic perspective on the JET-ILW pedestal, 2017. ISSN 17414326.

[52] D. R. Hatch, M. Kotschenreuther, S. M. Mahajan, G. Merlo, A. R. Field, C. Giroud, J. C. Hillesheim, C. F. Maggi, C. Perez Von Thun, C. M. Roach, and S. Saarelma. Direct gyrokinetic comparison of pedestal transport in JET with carbon and ITER-like walls. *Nuclear Fusion*, 59(8), 2019. ISSN 17414326. doi: 10.1088/1741-4326/ab25bd.

[53] Lorenzo Frassinetti, Christian Perez von Thun, Benjamin Chapman, Alexandre Fil, Jon

Hillesheim, Laszlo Horvath, Guido Huijsmans, Hampus Nyström, Vassili Parail, Samuli Saarelma, Gabor Szepesi, Bruno Viola, Rennan Bianchetti Morales, Mike G Dunne, Anthony Robert Field, Joanne Flanagan, Josep Maria Fontdecaba, David R Hatch, Bart Lomanowski, Costanza F Maggi, Sheena Menmuir, Stanislas Pamela, Colin M Roach, Elisabeth Rachlew, and Emilia R Solano. Role of the separatrix density in the pedestal performance in deuterium low triangularity JET-ILW plasmas and comparison with JET-C. *Nuclear Fusion*, 2021. URL http://iopscience.iop.org/article/10.1088/1741-4326/ac3363.